A study on slip activation for a coarse-grained and single crystalline CoCrNi medium entropy alloy

W. Abuzaid[1,*], L. Patriarca[2]

[1] *Department of Mechanical Engineering, American University of Sharjah, PO Box 26666, Sharjah, United Arab Emirates*

[2] *Politecnico di Milano, Department of Mechanical Engineering, via La Massa 1, 20156 Milano, Italy*

**Corresponding author* wabuzaid@aus.edu

Abstract: The new CoCrNi medium entropy alloy (MEA) has emerged to be one of the most promising systems which provide extraordinary ductility and strength at cryogenic temperatures. In this study, utilizing both polycrystalline and single crystal specimens, as well as advanced optical strain measurements, the deformation mechanisms dictating the mechanical behavior at the onset of plasticity were detected and precisely quantified. Independent of deformation temperature, the accumulation of permanent strains at the microstructural level was attributed to plastic slip at the onset of yielding and at low levels of deformation (< 10%). The resolved shear stress for slip activation was measured to be 78MPa at 298K and between 140MPa and 160MPa at 77K. These unique measurements were used to provide an estimate of the temperature dependent resolved shear stress for slip at temperatures ranging from 77K to 575K. In addition, strain heterogeneities at the grain-scale were measured to study the nucleation of slip at the micro-scale in polycrystalline specimens. In summary, the present study aims to quantitatively assess the accumulation of plastic strain and reveal the underlying deformation mechanisms (i.e., slip or/twinning) leading to the buildup of plastic strains at the microstructural level.

Keywords: *Medium entropy alloy, CoCrNi, single crystal, plastic deformation mechanisms, digital image correlation, critical resolved shear stress*

1. Introduction

Multicomponent high entropy alloys (HEA) alloys have attracted significant research interest and opened new avenues to achieve superior properties through alloying with relatively large number of base elements [1,2,11–13,3–10]. Initial efforts have focused on equiatomic HEAs composed of 5 or more elements. To date, the most commonly studied composition is the equiatomic FeCoCrNiMn alloy which is commonly referred to as the Cantor alloy [14]. This single phase alloy exhibits superior mechanical properties, particularly at cryogenic temperatures where simultaneous enhancement in strength and ductility were reported [1]. This phenomenon has been a subject of intense investigation over the last decade, in particular to reveal the underlying mechanisms which induce such a remarkable deviation from known trends in steels and metallic alloys [15,16,25–27,17–24]. Many other compositions have also been proposed as researchers started to explore the use of different elements and challenge the notion that HEAs with 5 or more elements are essential for enhanced properties [28]. More recent studies have in fact shown superior mechanical properties in CoCrNi, which is a medium-entropy alloy (MEA), that surpasses that of the Cantor alloy [15,28–35]. This system exhibits higher strength and hardening rate values and demonstrates exceptionally high fracture toughness especially at cryogenic temperatures [15]. Various studies have attributed these desirable properties to the activation of nano-twinning, particularly at low deformation temperatures, which induces additional hardening and delays the onset of necking [29,36,37]. With such exceptional set of properties over a wide temperature range, the CoCrNi system is expected to have significant promise in temperature sensitive applications. This motivates further research to better understand the source of these enhanced properties and the different microstructural aspects which influence the response of this alloy system.

The equiatomic CoCrNi MEA has a single phase with face-centered cubic (fcc) structure. The initial studies on this alloy system have reported high strength and ductility levels resulting in fracture toughness values exceeding 200 MPa√m and a remarkable 275 MPa√m at cryogenic temperatures [1,34]. The ductility enhancement has been typically associated with the activation of nano-twinning as an additional deformation mechanism. In addition, twin boundaries act as barriers for dislocation motion which consequently lead to higher work hardening rates resulting in the extraordinary combination of ductility and strength [29,36–38]. Initial observations of deformation twinning has been reported at strain as low 4% in single crystalline specimens [38] while in polycrystalline form, Laplanche and coworkers found nano-twinning activation above 4.0% at 77K and above 9.7% at 293K [29]. At 77K, twinning was reported at lower strain levels due to the increase in slip resistance at lower temperatures which allows the material to reach the critical twinning stress earlier. In general, such fundamental observations have been made using transmission electron microscopy (TEM) post deformation to different strains levels and at different deformation temperatures. However, there is still limited insight into how the selective activation of slip and twinning contributes to plastic strain localization at the microstructural level. More specifically, full-field strain measurements focused on the deformation heterogeneities in the vicinity of grain boundaries, in particular at cryogenic temperatures, remains limited for CoCrNi MEA. A better understanding of the local buildup of plastic strains, i.e., how much slip and twinning affect the strain localizations, would provide further insight into the response of this alloy system and bridges the gap between macroscale bulk response measurements and analysis conducted at the microstructural level using TEM.

The experimental approach presented in this study is based on detailed local strain maps measured with full-field, high-resolution digital image correlation (DIC). Several studies have

shown the importance of quantifying sub-grain strains in detecting the active deformation mechanisms which control the mechanical behavior of metallic alloys [24,39]. For example, Carroll and coauthors measured the plastic strain accumulation with grain level resolution in the proximity of a propagating crack in Hastelloy X [40] and for the same alloy, Abuzaid and coworkers detected the origin of fatigue cracks at specific grain boundaries using high-resolution DIC measurements [41]. Full-field DIC measurements have also been utilized to shed insight into the orientation-dependence of slip for single and oligo-crystal microstructures and to compare with numerical simulations [42]. These studies demonstrated how the local microstructure activates specific deformation mechanisms which successively determine the level of strain localization and deformation heterogeneity. The proper quantification of the strain heterogeneities is fundamental to understand the role of the microstructure in the mechanical behavior of the considered alloy. In this study, DIC was further enhanced for sub-grain strain measurements at 77K for the present CoCrNi MEA. The strains were measured in specific experiments where the same microstructure was deformed at cryogenic temperature and successively at room temperature. The local strains were characterized for both deformation steps and analyzed in view of the grain orientation. This specific experimental set-up, sometime referred to as the Cottrell-Stokes loading [43], enabled a direct and unambiguous assessment of the effect of deformation temperature on the local deformation mechanisms during the onset of plasticity for the same CoCrNi microstructure.

For both polycrystalline and single crystal specimens, DIC was also used to pinpoint the onset of local plastic deformation. The high resolution experimental measurements, along with Electron Back Scatter Diffraction (EBSD) grain orientation data were utilized to determine fundamental material properties as, for example, the activated deformation mechanism (i.e., slip or twinning) and the associated critical resolved shear stress. The determination of the τ_{CRSS} for

slip and twinning is of fundamental importance to understand the mechanical behavior and to pursue modelling efforts. In particular, the relative magnitudes of τ_{CRSS} for slip and twinning, and their temperature dependence, dictates how plastic deformation is accommodated at certain deformation temperatures and strain/stress levels. This in turn affects the attained strain hardening rates, strength, and ductility. Careful experimental determination of $\tau_{CRSS\text{-}slip}$ for slip in the HEA Cantor alloy has revealed a strong temperature dependence with an increase from 70 MPa to 175 MPa at 77 K [39]. It should be noted that although such a response is expected in bcc alloys, it unusual in fcc structures. In the case of twinning, magnitudes between 153 and 235 MPa were reported for $\tau_{CRSS\text{-}twin}$ at 77K [24,29]. At room temperature (i.e, 298 K), Laplanche et al. concluded that $\tau_{CRSS\text{-}twin}$ is temperature independent and twinning would therefore only occur at very high strains close to fracture [29]. A similar observation has been made in the case of CoCrNi reporting a $\tau_{CRSS\text{-}twin} = 260$ MPa, independent of temperature. As observed, twinning occurs at higher stresses than slip and its detection is based on interrupted tests where TEM or/and high resolution EBSD were carried out. It should be pointed out, however, that although such careful experimental efforts provide deep insight into the microstructure and clear evidence of twinning and slip, the pinpointing of the critical stress $\tau_{CRSS\text{-}slip}$ is generally performed by observing the deviation from linearity of the single crystal stress-strain behavior. Therefore, this methodology can be used as a first approximation. In this work we utilize in-situ local stress-strain curves measured by high-resolution DIC to precisely detect the slip onset, and consequently $\tau_{CRSS\text{-}slip}$, in both polycrystalline and single crystal specimens. By using such experimental approach, on both single crystalline and polycrystalline specimens, and across a wide range of temperatures, the work clearly identifies the onset of slip and the corresponding CRSS, and demonstrates that the onset of plastic slip occurs well below the macroscopic stress level at which deviation from linear elastic behavior is observed.

The results were also utilized to outline the fundamental temperature dependency of $\tau_{CRSS\text{-}slip}$ across a wide temperature range (77 – 573K) which has not been established in the literature for the CoCrNi MEA.

In summary, the mechanical behavior of coarse-grained and single crystal CoCrNi MEA was investigated in this work with focus on the deformation mechanisms at the onset of plasticity for temperatures ranging from 573K to cryogenic (77K) deformation temperature. The microstructure of the CoCrNi alloy is presented in Section 2, while Section 3 focuses on the experimental results. In particular, in Section 3.1 the mechanical properties at 298K and 77K are briefly summarized. Successively, Section 3.2 illustrates the local strain heterogeneities quantified using the combination of high-resolution DIC and EBSD grain orientations for both 298K and 77K temperatures. The measurements of $\tau_{CRSS\text{-}slip}$ for both polycrystalline and single crystal are described in Section 3.3, while in Section 3.4 we discuss the temperature-dependence of the yield stress σ_Y and $\tau_{CRSS\text{-}slip}$. Finally, the discussion of the results is included in the Section 4.

2. Materials and Methods

The CoCrNi equiatomic medium entropy alloy was arc-melted using pure elements (purity > 99.5 wt%). Following casting, the ingot was homogenized at 1200 ºC for 24 hrs in an Ar atmosphere. The nominal composition and homogeneity of the ingot was confirmed using EDX as shown in Fig. 1. Tensile specimens were subsequently machined from the homogenized ingot using electric wire EDM. The dog-bone samples had a 3 × 1.5mm cross section and 8mm gauge length. Prior to loading, all specimens were solution heat treated at 1200 ºC for 1hr followed by quenching in oil to assure a single phase, face-centered cubic (fcc) structure. This was confirmed using X-Ray diffraction (XRD) as shown in Fig. 2 and electron backscatter diffraction (EBSD) as will be shown

in the Results section. Based on the XRD peaks, the calculated lattice parameter was found to be $a = 3.55$Å.

Tensile experiments were conducted at various deformation temperatures, both in-situ and ex-situ. In general, the in-situ strain measurements were collected using lower-resolution digital image correlation (DIC) for room temperature (RT) and elevated deformation temperatures (up to 573K). For the sub-zero experiments, in-situ strain data was collected using a 5 mm gauge length extensometer. In addition to in-situ measurements, high resolution (sub-micron strain measurement resolution ≈ 0.88 μm/pixel) strain measurements were conducted on selected samples to study the local deformation response in relation to the microstructure. In this case, optical microscopy was used to collect reference and deformed images for high resolution DIC following the procedure detailed in [44]. All ex-situ measurements were conducted following unloading and at room temperature (note that deformation temperatures still vary).

An Instron load frame (for most specimens) and a micro-loading stage (for high-resolution in-situ measurements) were used to apply the tensile loading. For experiments conducted at 77K, the entire sample, loading grips, and extensometer were submerged in a liquid nitrogen (LN) bath prior to loading and throughout the deformation cycle. For the experiments conducted at 193K, a low temperature environmental chamber was used in conjunction with an external source of liquid nitrogen. For the high temperature experiments, an environmental chamber was utilized for heating. For all the experiments, loading was initiated after a 20 min soaking time at the desired deformation temperature. In all cases, deformation was applied using displacement control with an average strain rate of $\approx 2^{-4}$ s^{-1}.

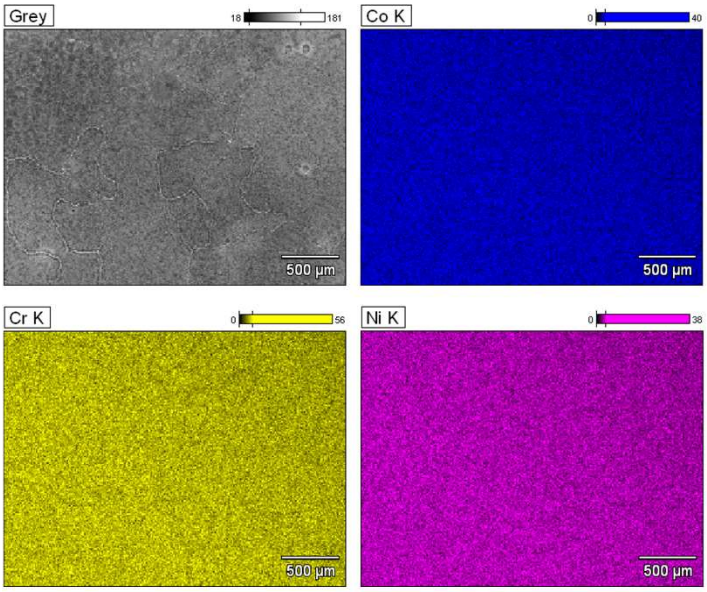

(a)

Co (at.%)	Cr (at.%)	Ni (at.%)
33.8	32.3	33.9
Co (wt.%)	**Cr (wt.%)**	**Ni (wt.%)**
35.2	29.7	35.1

(b)

Fig. 1. (a) EDX maps of Co, Cr, and Ni confirming the ingot's homogeneity. (b) The nominal composition in wt. % and at. %.

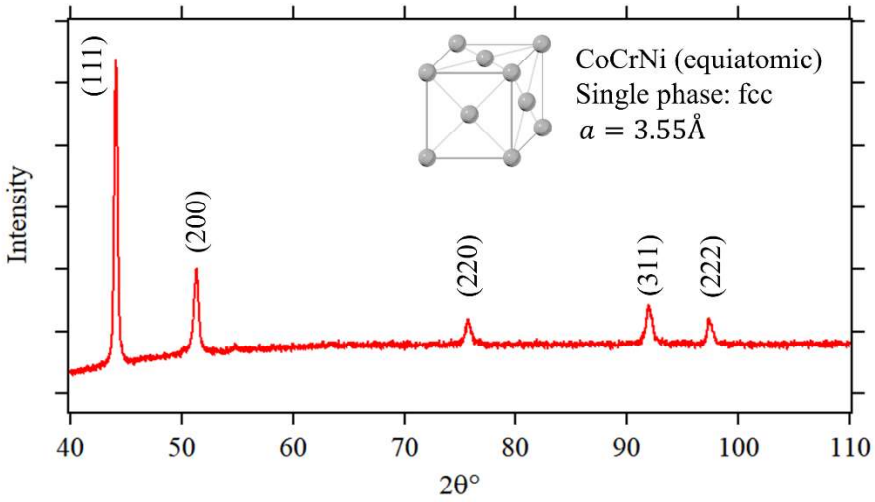

Fig. 2. XRD analysis of CoCrNi specimens following homogenization and solution heat treatments. The results point to a single fcc phase with a lattice parameter $a = 3.55$ Å.

Results and Analysis

3.1 Mechanical properties at cryogenic and room temperature

Figure 3a shows a comparison of the stress-strain response (up to 40% strain before unloading) for the fully-recrystallized and coarse grained (CG) CoCrNi MEA considered in this work. The representative curves clearly highlight the expected enhancement in strength, without scarifying ductility, for this class of alloys at cryogenic temperatures. This macro-scale comparison of the deformation behavior does not point to any major changes in the dominating deformation mechanism due to the change in deformation temperature. The strain-hardening behavior presented in Fig. 3b points to a slightly higher strain hardening rate at the early stages of deformation for 77K deformation temperature. However, at higher strains, the strain hardening rates are similar. The activation of deformation twinning, in addition to slip, has been reported for this alloy system at 77K which can contribute to the slightly higher hardening rates at this deformation temperature [29,36,37]. However, it is noted that after the sharp drop in strain hardening rate in Stage I, the reduction rate decreased in Stage II, which is typical for slip mediated plasticity. This suggests that the deformation up to this stage was still dominated by plastic slip rather than twinning. In Stage III, the hardening rate started to increase which can be triggered be the activation of deformation twinning as an additional deformation mechanism. These effects proceed up to Stage IV where saturation takes place and the hardening rate starts to drop.

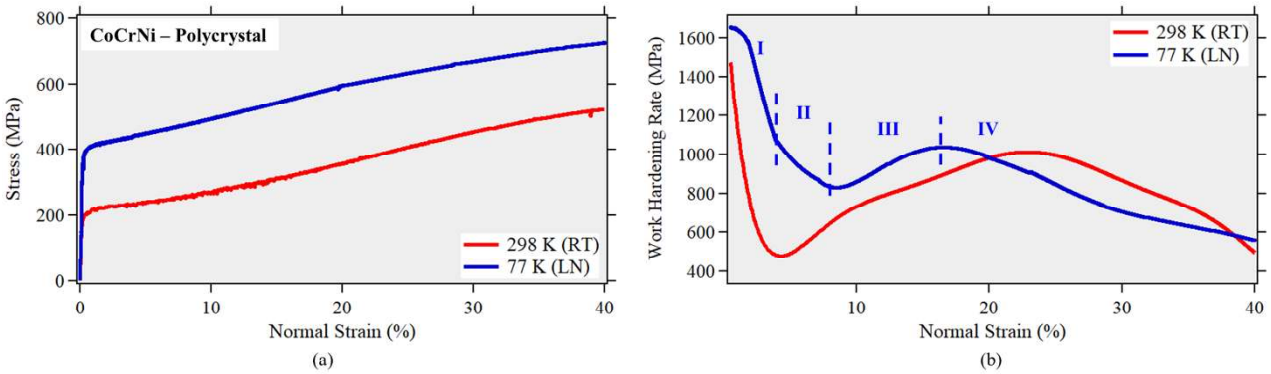

Fig. 3. (a) Representative stress-strain response of CoCrNi samples deformed at 77 and 298 K. (b) The corresponding strain-hardening rate.

3.2 Active deformation mechanisms at the onset of plasticity

As explained earlier, this work is focused on investigating the global and local material response at low levels of deformation in CoCrNi (i.e., <10% plastic strain). Using high resolution strain measurements at the microstructural level, the localizations and accumulation of local plastic strains were investigated at room (298K) and cryogenic temperatures (77K). To enable a direct comparison between the local accumulation of plastic strains for the considered deformation temperature, any differences induced by microstructural variation (i.e., grain orientation) has to be eliminated. This was achieved by conducting high-resolution DIC strain measurements on single specimens deformed plastically at both of the considered deformation temperatures. In the first deformation cycle, the specimen was subjected to ≈ 3% plastic strain at 77K. Following unloading, another loading cycle was applied at the other temperature extreme (298K). For both deformation increments, high-resolution DIC was utilized to quantify plastic strain accumulation in relation to the local grain orientation which was determined using EBSD.

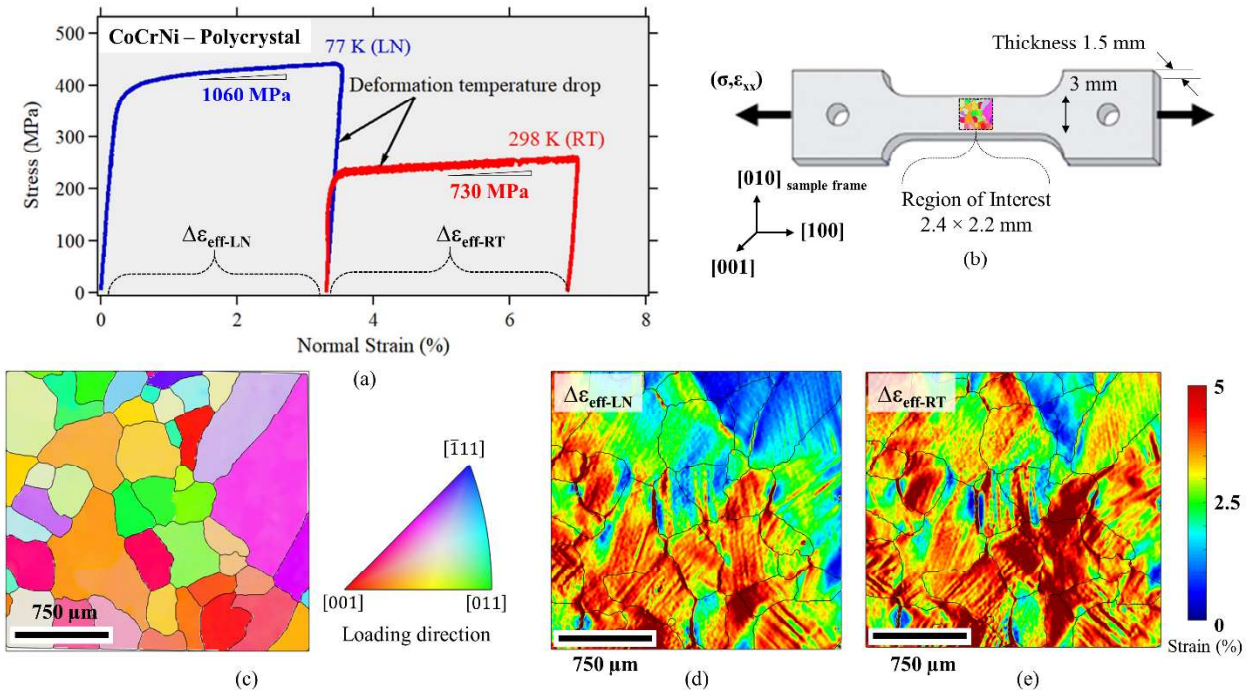

Fig. 4. (a) Stress-strain curves for a CoCrNi specimen subjected to two loading increments at different deformation temperatures 77 and 298 K. (b) The region in interest on the sample's surface. (c) EBSD grain orientation map in the region of interest outlined in (b). (d) – (e) High resolution strain contour plots showing the residual strain field in the region of interest following deformation at 77 K and 298 K, respectively.

Figure 4a shows the global stress-strain curves obtained following the "*temperature jump*" experiment described above. The microstructure in a roughly 2.4 × 2.2 mm^2 area on the sample's surface is shown in Figs. 4b-4c. The plastic strain field (effective plastic strain ε_{eff}) in relation to the local microstructure (i.e., within grains and in the vicinity of grain boundaries) for the 77K loading cycle is shown in Fig. 4d. Following the first deformation cycle, another EBSD scan was collected in the region of interest. The collected results and grain orientation map were almost identical to the EBSD data prior to deformation. No signs of any clear twinning activity were detected which would therefore lead to the conclusion that the local buildup of permanent strains in Fig.4d was induced by mainly plastic slip rather than deformation twinning. This was again observed in the second deformation cycle which was conducted at 298K, as shown in Fig. 4e. The

local residual strain field was almost identical for both deformation temperatures (notice the similarities in activated grains and localization in GB regions). Full statistical analysis of the residual strain fields for the considered deformation temperatures is shown in Figs. 5a-5c. The histograms in Fig.5a were determined by normalizing the local effective plastic strain measurements with the average value calculated separately for the two deformation steps. The experimental data were observed to follow a normal distribution as depicted in the normal probability plots included in Fig. 5b. The results again support the visual observation of similar deformation response from the strain contour plots presented in Figs. 4d-4e. However, it is noted that the standard deviation decreased slightly in the second load step performed at 298K indicating a slightly more uniform contribution to the deformation associated with each grain. From a crystallographic point of view, the distribution of the maximum Schmid factors for slip and twinning in the region of interest differs significantly as shown in Fig. 5c. Moreover, the maximum Schmid factor histogram for slip shows that the values are all contained in the interval between 0.4 and 0.5. This indicates that all the grains possess at least one slip system with a minimum Schmid factor of 0.4 suggesting that based on crystallographic analysis, slip is favored over twinning at the onset of plasticity for the considered microstructure. At 77K, according the values reported in literature for the critical resolved shear stress for twinning $\tau_{CRSS\text{-}twin} = 260 \pm 30$ MPa [29], twinning should activate when the global stress is at least 520±60MPa (using a $SF_{twin} = 0.5$). This stress level was not achieved in the applied loading cycles and the DIC local strain measurements do not point to any clear evidence of twin activation. If deformation twinning had a significant contribution on the deformation response at 77K deformation temperature, then the contour plots reported in Fig. 4 and strain distribution in Fig. 5 would differ significantly from the results obtained at 298K where slip is known to dominate. However, such difference was not observed,

and the results support the observation that plastic slip dominated the deformation response at these low levels of deformation, regardless of the deformation temperature.

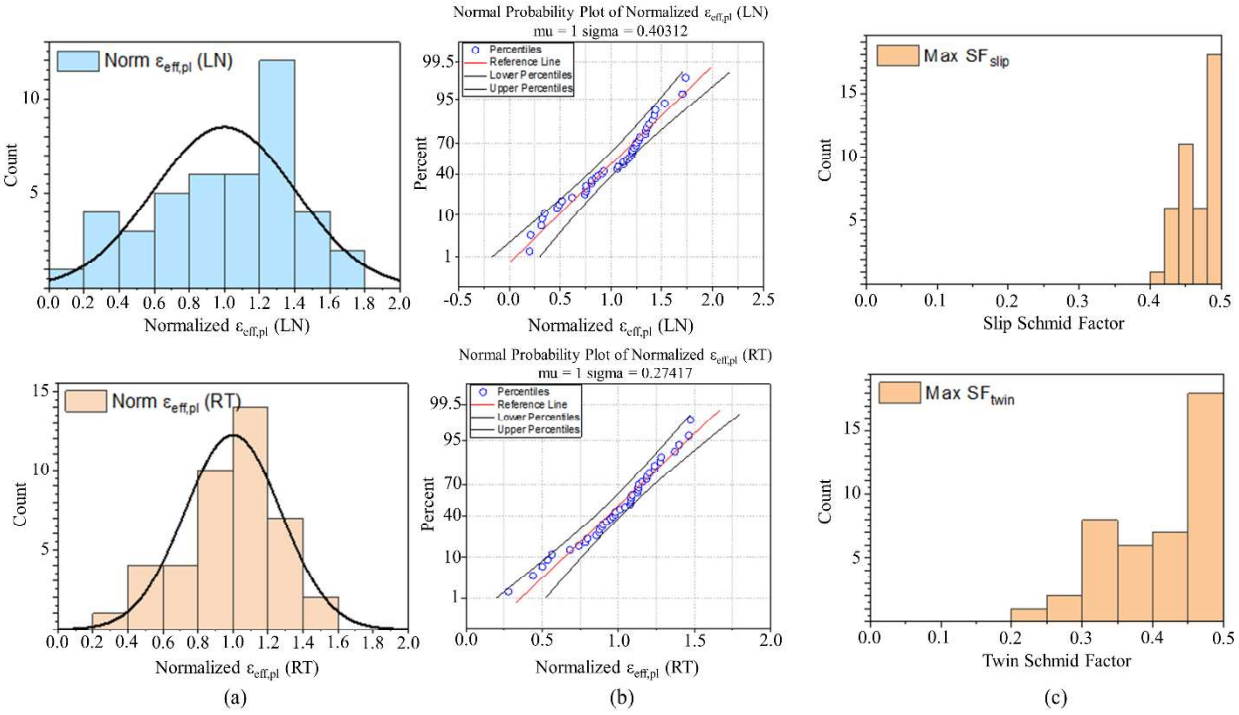

Fig. 5. (a) Histograms of the normalized effective plastic strains for the loading steps performed at 77K and successively at 298K. (b) The associated normal probability plots indicate that the distribution of the normalized effective plastic strains can be modelled with a normal distribution with an average value of 1 and standard deviation equal to 0.403 at 77K and 0.274 at 298K. (c) Histograms of the maximum Schmid factors for slip and twinning determined from the EBSD map showed in Fig. 4c.

To further confirm the observations made from the previous specimen, which was deformed at 77K first and then subjected to another loading cycle at 298K, another sample was investigated in a reverse loading sequence (i.e., the first deformation cycle at 298K followed by another cycle at 77K). The stress-strain curves and the corresponding high-resolution residual strain fields are presented in Fig. 6. Again, the local strain accumulation, activated grains, and localization in the vicinity of GBs were observed to be similar despite the difference in deformation temperature. The

results support the previous observation of slip mediated plasticity at the deformation levels considered in this work (i.e., < 10%).

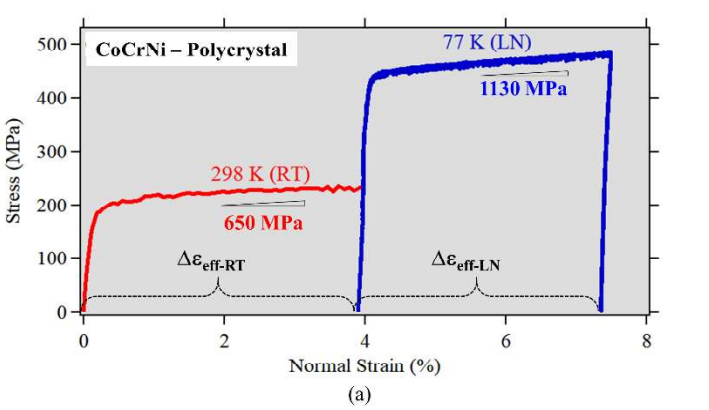

(a)

Deformation Temperature	Average Strain (%)	Stdv. of the field normalized by the average strain
298 K (RT)	3.9	0.41
77 K (LN)	3.0	0.40

(c)

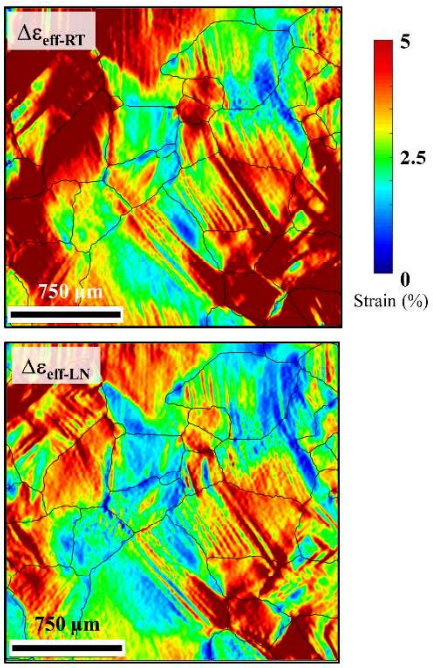

(b)

Fig. 6. (a) Stress-strain curves for a CoCrNi specimen subjected to two loading increments at different deformation temperatures 298 and 77 K. (b) High resolution strain contour plots showing the residual strain field in the region of interest following deformation at 298 K and 77 K. (c) Statistical analysis of the deformation strain fields showing the field average strain and standard deviation.

3.3 Critical resolved shear stress for slip

As concluded from the previous section, slip dominates the deformation response of the medium entropy alloy, CoCrNi, at low levels of deformation. It is therefore important to quantify the critical resolved shear stress (τ_{CRSS}) for the activation of slip. Accurate quantification of this fundamental quantity is very important for material modeling efforts. In this work, the τ_{CRSS} was determined utilizing high resolution in-situ strain measurements. Both polycrystalline and single crystal specimens were utilized to confirm the measured critical stress. Fig. 7a shows the stress-strain curve of a polycrystalline sample deformed plastically to about 4% strain using a micro-loading stage. An EBSD grain orientation map showing the microstructure in the region of interest is shown in Fig. 7b. Reference and deformed images for DIC measurements were captured using an optical microscope (0.44μm/px). The loading was paused, without unloading, at several locations (marked as A, B, C, and D as shown in Fig. 7a) to capture deformed images. To cover the entire region of interest, 4 images were collected and stitched following the procedure detailed in [44]. The corresponding strain contour plots for the points marked in Fig. 7a are shown in Fig. 7c. At a global/nominal stress level of ≈ 100MPa (i.e., point A), the full-field deformation measurement point to elastic response and no signs of slip activation. At point C, clear accumulation of plastic strains and localizations in particular grains can be observed. However, earlier indications of activation of slip can be traced back to point B which was captured at a nominal stress of 193.7MPa. It is noted that following this method, both the stress levels (i.e., 193.7MPa in this case) and the activated grain/s can be determined, which is essential for the calculation of τ_{CRSS}. However, this requires knowledge of the activated slip system which can be determined using either slip trace analysis or using the localized strain bands.

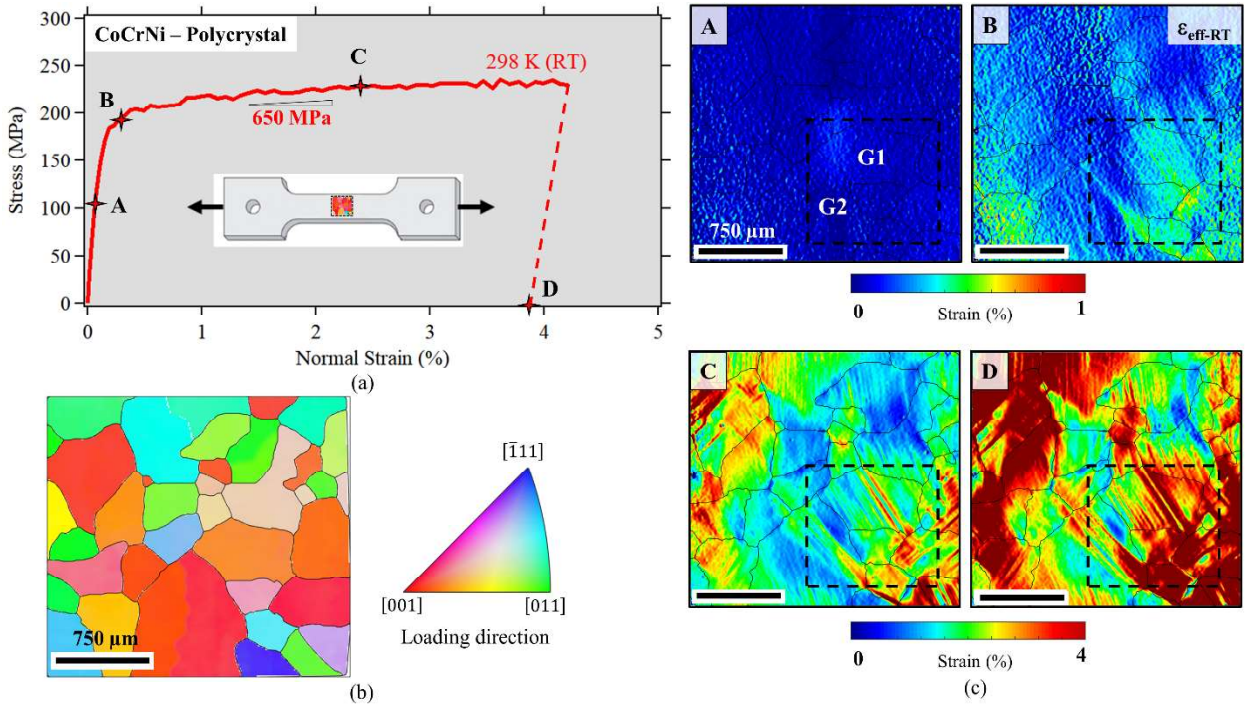

Fig. 7. (a) Stress-strain curve for a CoCrNi specimen deformed plastically at 298 K using a micro-loading stage to allow for high resolution in-situ strain measurements. (b) EBSD grain orientation map in the region of interest outlined in the inset in (a). (c) High resolution strain contour plots of the effective plastic strain at different levels of deformation A, B, C, and following unloading at D. The stress levels for each of the contour plots is marked on the stress-strain curve shown in (a).

The early signs of slip activation were observed in Fig. 7c (state B). The activated region is outlined with a dashed black line and encompasses several grains. The grain orientation map and DIC strain contour plots in the activated region is enlarged and shown in Fig. 8. In addition, an optical image in the same region following unloading is presented. The slip traces in the plastically deformed region are clearly observed from the high resolution DIC map (seen as localized strain bands) and the traces in the optical image. Utilizing the grain orientations of the two largest grains in the outlined region (i.e, grains G1 and G2), the traces in both grains were identified to match the $(\bar{1}11)$ slip plane which is shared by 3 fcc slip systems. The slip system

having the highest Schmid factor was assumed to be active as shown in Fig. 8. Based on this slip trace analysis, the activated slip systems were the $(\bar{1}11)[01\bar{1}]$ in G1 which has a Schmid factor of 0.48 and the $(\bar{1}11)[01\bar{1}]$ in G2 which has a Schmid factor of 0.45. Using the nominal stress level of 193.7 MPa at point B, where slip was initially observed, the CRSS for slip activation can be calculated as 93 and 87 MPa in Grains G1 and G2, respectively. The lower CRSS magnitude from G1 and G2 (i.e., 87 MPa) was used to obtain an estimate of $\tau_{CRSS\text{-}slip}$. In addition, to account for the possibility that slip activation took place slightly before the measurement point at B (i.e., at a stress < 193.7 MPa), the critical stress for slip activation from this experiment is reported to be $\tau_{CRSS\text{-}slip} \leq 87$ MPa.

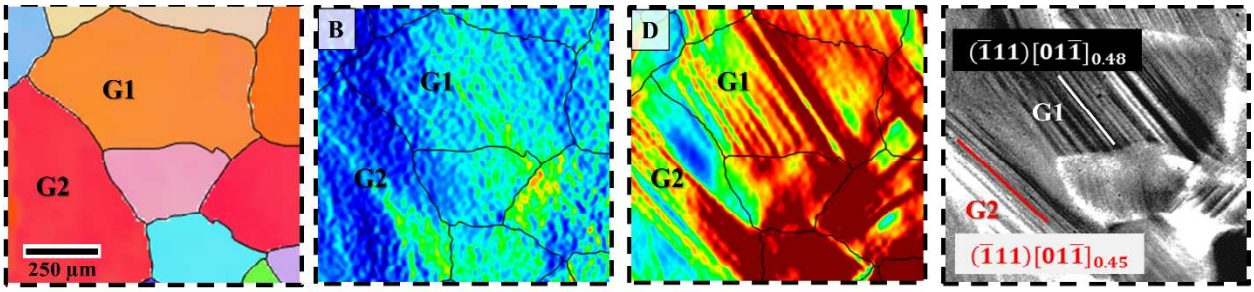

Grain G1			Grain G2		
Euler angles (Bunge)	φ_1	168	Euler angles (Bunge)	φ_1	167
	ϕ	171		ϕ	163
	φ_2	245		φ_2	252
Slip trace plane (observed)		$(\bar{1}11)$	Slip trace plane (observed)		$(\bar{1}11)$
Potential Slip System		Schmid Factor	Potential Slip System		Schmid Factor
$(\bar{1}11)[101]$		0.12	$(\bar{1}11)[101]$		0.07
$(\bar{1}11)[110]$		0.36	$(\bar{1}11)[110]$		0.37
$(\bar{1}11)[01\bar{1}]$		**0.48**	**$(\bar{1}11)[01\bar{1}]$**		**0.45**

Fig. 8. Grain orientation map, DIC strain fields at points B and D, and slip trace analysis for the region marked in Fig. 7c. Initial slip activity was detected in grains G1 and G2. The value of the τ_{CRSS} was determined using the minimum resolved shear stress for the activated slip system in grain G2. Slip traces were used to determine the activated slip plane. The system with the highest Schmid factor was assumed to be active. Grain orientations and Schmid factor calculations are presented in the table.

In order to establish a more accurate measurement of the CRSS for slip, a single crystalline specimen of CoCrNi was investigated. The sample was loaded plastically at 298K, in tension, along the [001] crystallographic direction as shown in Fig. 9a. Two loading increments were applied, the first up to 0.23% strain and then unloaded (point A in Fig. 9a). Subsequently, the sample was subjected to a second loading cycle up to 5.5% strain and unloaded to point B. Full field DIC strain measurements were collected in-situ during loading at a relatively low magnification (2μm/px) and ex-situ, at points A and B, at very high magnification (0.35μm/px). The high resolution strain contour plots, shown as insets in Fig. 9a, allow for clear and accurate assessment of the activated slip system. Based on the observed slip bands, the activated slip was determined as the $(1\bar{1}1)[110]$ which has a Schmid factor of 0.42. The in-situ, low magnification, strain contour plots where collected throughout the loading cycle (representative cases at points A and B are shown in Fig. 9c) which allows for capturing the instance of slip activation during loading. Figure 10a shows the stress-strain curve generated using the in-situ strain measurements. The black curve represents the bulk sample response as shown also in Fig. 9a (first loading cycle $\varepsilon = 0.23\%$). The red curve was extracted from local strain measurements in the region where slip was activated as shown in Fig. 10b. As expected, the local strain magnitudes are significantly higher than the bulk strain at the same stress level. Utilizing the local stress-strain curve and a 0.05% strain offset, the local yielding stress was determined to be 186 MPa. It's noted that at this point, marked with red circle in Fig. 10a, the bulk stress-strain curve is still in the linear elastic region. Once both the nominal stress level at yield and the activated slip system were determined, $\tau_{CRSS\text{-}slip}$ was calculated to be 78.1 MPa. This magnitude of $\tau_{CRSS\text{-}slip}$ was less than the 87 MPa magnitude which was estimated using the polycrystalline specimen and a discretized load step sequence.

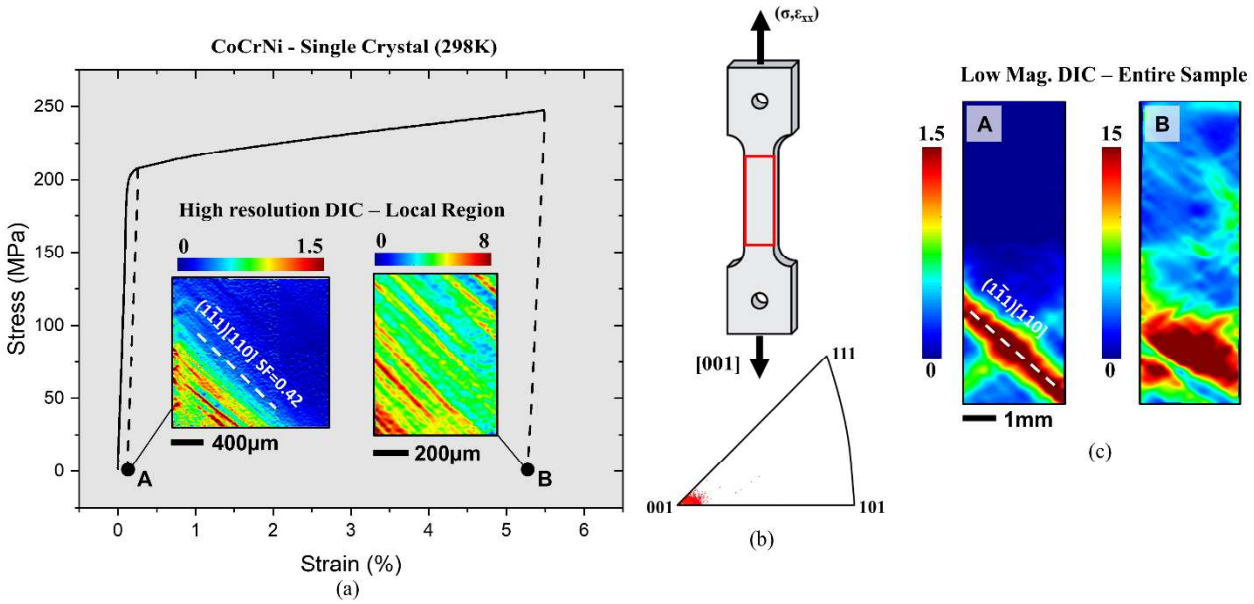

Fig. 9. (a) Stress-strain curve of a single crystalline specimen loaded in tension. The sample was unloaded to point A, reloaded, and unloaded to point B. The high-resolution strain contour plots shown as insets were collected following unloading. (b) Sample schematic and the stereographic triangle showing the crystal orientation along the loading direction. (c) in-situ strain contour plots covering the entire gauge length at points A and B.

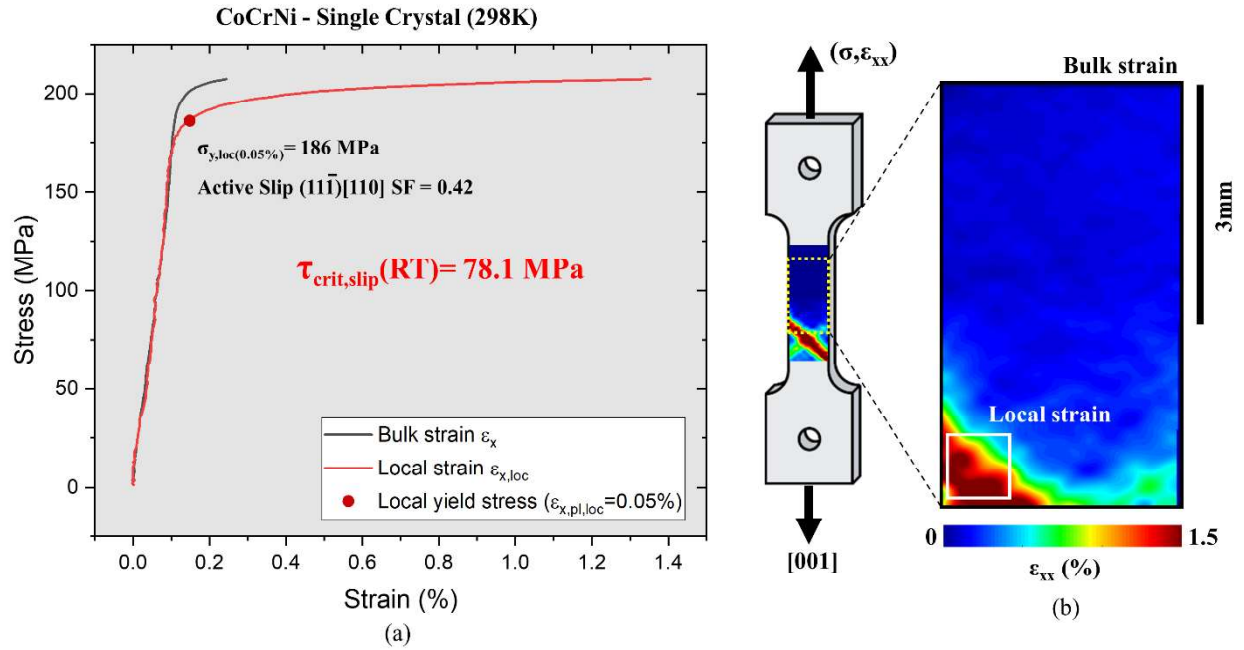

Fig. 10. (a) Stress-strain curve of a single crystalline specimen loaded in tension. The bulk strain across the entire gauge section were used to construct the black curve. The localized strains in a small region where slip initially initiated were used to construct the red curve. (b) A representative strain contour plot captured in-situ. The average strain in the entire region represents the bulk strain while the strain the region highlighted with white box represents the local strain. Initiation of slip was detected in the local region during loading.

A second single crystal specimen with loading direction along the [5 1 10] directions was tested at 77K. To enable the detection of slip initiation at this temperature, a stable speckle pattern was applied on the specimen surface and the reference images were captured at room temperature under an optical microscope with a resolution of 0.44µm/px. The area analyzed with high-resolution DIC is outlined with a black box in Fig. 11b. A total of four images were captured and successively stitched to cover a region of interest sufficiently large to capture local strain bands. Prior to loading, an EBSD scan was performed to measure the single crystal orientation. The grain orientation map and stereographic triangle are shown in Fig. 11b.

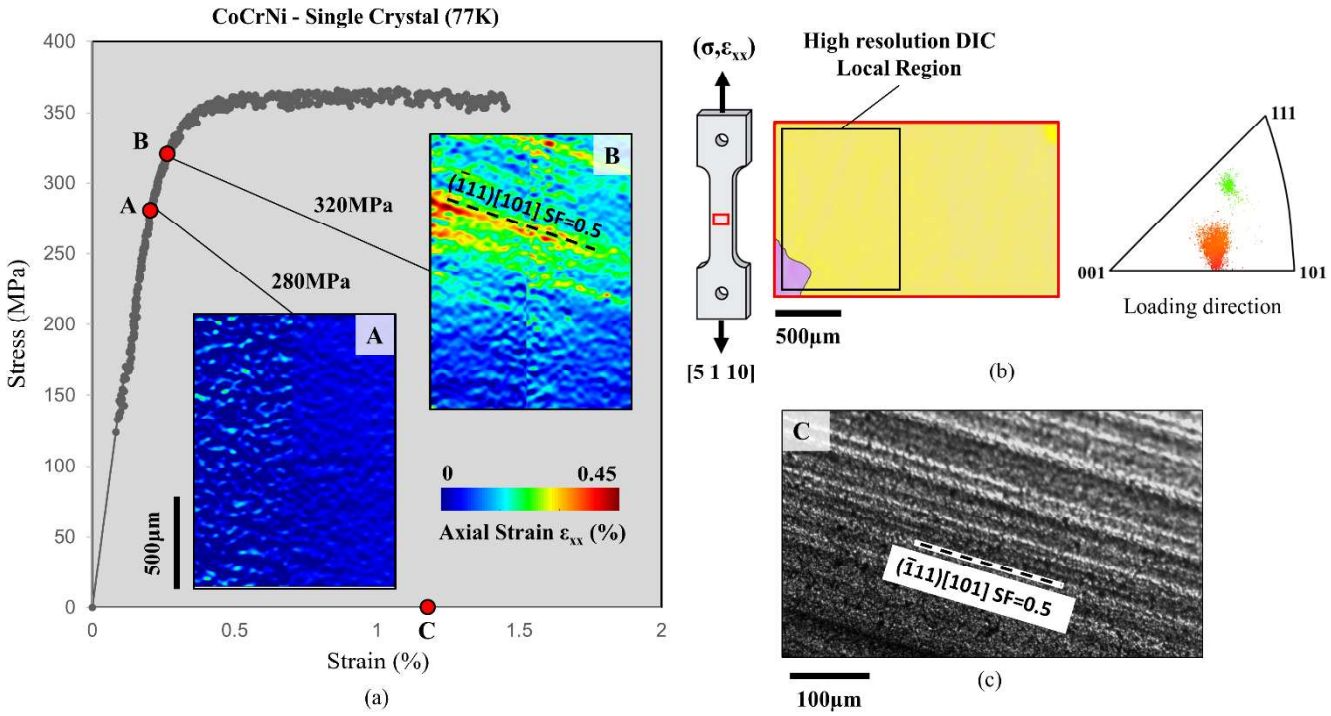

Fig. 11. Stress-strain curve of a single crystalline oriented along the [5 1 10] orientation and loaded at 77K. (a) High-resolution DIC was performed ex-situ after loading the specimen at 280 MPa and 320 MPa stress levels; the contour plot captured at 320MPa shows preferential slip bands oriented according the $(\bar{1}11)[101]$ slip system with the largest Schmid factor; (b) the EBSD map and the stereographic triangle of the specimen area under investigation; (c) detail of the slip traces on the specimen surface.

The experiment was conducted initially in load control using a multi-step loading-unloading procedure. At each interruption, the specimen was unmounted from the load frame and the images for DIC were taken under the optical microscope. Prior to test, we considered an initial analysis of the slip systems with the largest Schmid factor and we found the potential slip systems to be $(\bar{1}11)[101]_{SF=0.5}$ and $(1\bar{1}1)[\bar{1}01]_{SF=0.47}$. Consequently, considering that the ratio between the 0.2% yield stress at 298K and at 77K is approximately 0.5 (see next Section for further details), we predicted the resolved shear stress at 77K to be approximately $\tau_{CRSS\text{-}slip,77K}$=156.6MPa. The corresponding nominal stress for slip activation for the single crystal under investigation is then expected to be $\tau_{CRSS\text{-}slip,77K}$/(SF=0.5) = 313.2MPa. According to this preliminary analysis, as shown in Fig. 11a, a nominal stress of 280MPa (point A) was initially applied. No plastic deformation developed after this load step as shown from the strain contour plot. The second load step (point B) was performed at a maximum stress of 320MPa. The DIC strain map clearly reveals the nucleation of shear bands which correspond to the slip traces parallel to the slip system with the largest Schmid factor $(\bar{1}11)[101]_{SF=0.5}$. Since the experiment was performed to discrete stress levels, we determined the resolved shear stress for slip nucleation at 77K to be in the interval $\tau_{CRSS\text{-}slip,77K}$ =140-160MPa.

3.4 Temperature dependence of $\tau_{CRSS\text{-}slip}$

As clearly shown in the previous section, the critical resolved shear stress has a paramount influence on the temperature dependence of the yield stress. In order to better understand this temperature dependence, additional tensile experiments were performed at various deformation temperatures to quantify the temperature dependent yield strength across a wide range of temperatures. Fig. 12 shows representative stress-strain curves determined for a maximum

deformation of 24%. The aim of the collected data in Fig. 12 is to utilize the yield strength measurements and the previously determined $\tau_{CRSS\text{-}slip}$ at 298 and 77K to estimate the CRSS for slip across a wide temperature range.

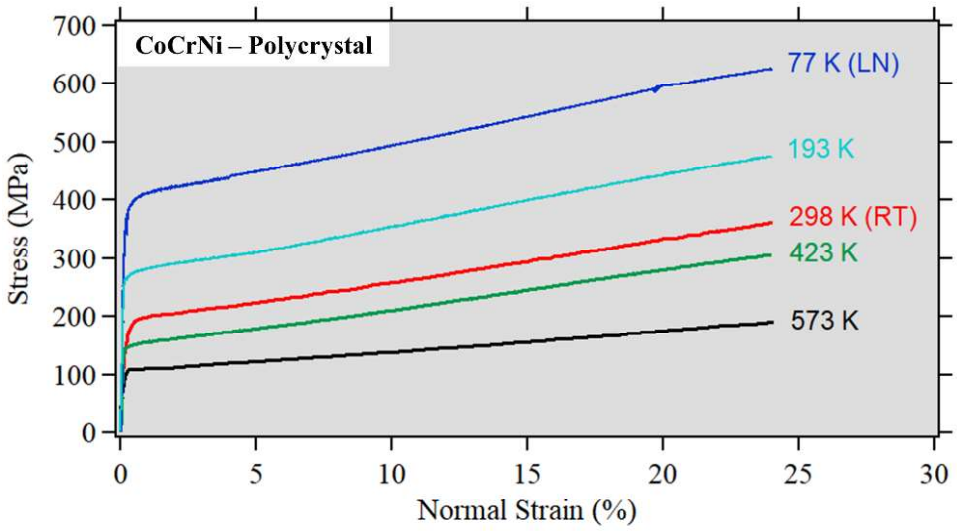

Fig. 12. Representative stress-strain curves at various deformation temperatures ranging from 77 – 573 K.

Tensile tests were repeated 2-3 times for each deformation temperature, and the yield strength values were determined using the 0.2% plastic strain offset. As shown by Wu and coauthors for the same composition [28], the dominant factor for yield strength temperature dependence is the Peierls stress. Other factors affecting the flow stress such as the initial dislocation density ($\Delta\sigma_{pi}$) and the precipitate hardening ($\Delta\sigma_{ppt}$) can be disregarded as the present alloy is studied in the solution-treated condition. The contribution coming from the solid solution ($\Delta\sigma_{ss}$) can be incorporated in the friction stress term (σ_{fr}) which is considered the main contributor to the temperature dependence. The additional strengthening introduced by the grain boundaries ($\Delta\sigma_{gb}$) is supposed to be temperature independent for the present coarse-grained microstructure. According to these assumptions, two main terms contribute to the yield stress for this alloy in the present solution treated state:

$$\sigma_Y = \sigma_p + \sigma_b \quad (1)$$

σ_b is the a-thermal stress term while σ_p is the Peierls stress. Based on these considerations, Wu and co-authors provided an exponential equation for the Peierls stress [28]:

$$\sigma_p = \frac{2G}{1-\nu} exp\left(\frac{-2\pi w_0}{b}\right) exp\left(\frac{-2\pi w_0}{b}\alpha T\right) \quad (2)$$

G is the shear modulus herein measured to be 67881 MPa, and the Poisson's ratio ν = 0.31 [28]. The ratio between the dislocation width at 0K and the Burgers vector magnitude w_0/b, and the parameter α were calculated using a proper fitting of the yield stress versus temperature data adopting a convenient fitting equation in the form of:

$$\sigma_Y(T) = \sigma_a exp\left(\frac{-T}{C}\right) + \sigma_b \quad (3)$$

Where $\sigma_a = \sigma_p(0K) = \frac{2G}{1-\nu} exp\left(\frac{-2\pi w_0}{b}\right)$ and $C = \frac{b}{2\pi w_0 \alpha}$. The resulting fitting of equation 3 is shown in Fig. 13a along with the 95% confidence bands. Based on provided results, the fitted material parameters were obtained to be $\alpha = 0.0007$, $\frac{w_0}{b} = 0.97$ and $\sigma_b = 68MPa$.

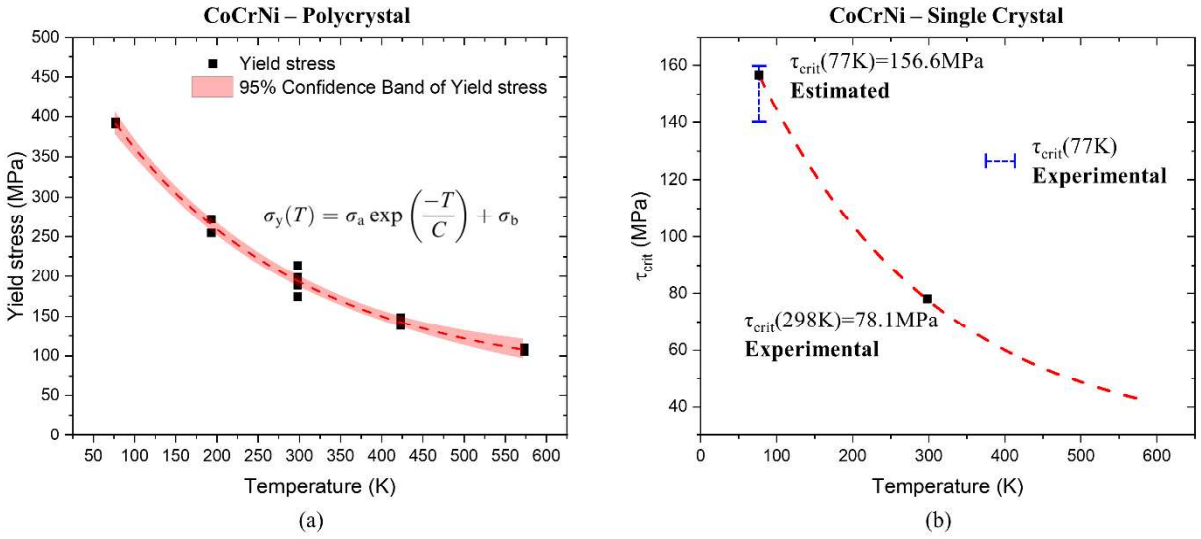

Fig. 13. (a) Temperature dependence of the yield stress and fitting of the experimental values according an exponential law (see text for more details). (b) Estimated temperature dependence of the CRSS according the value obtained at 298K.

As shown in the previous section, the measured critical resolved shear stress for slip at 298K from the test on the [001] single crystal is $\tau_{CRSS\text{-}slip,298K}$ = 78.1MPa. The 0.2% yield stress at the same temperature is 194.2MPa. To estimate the critical resolved shear stress in the 77K-575K range, we assume that, as a first approximation, the ratio $\tau_{CRSS}/\sigma_{Y,0.2\%}$ is constant and calculated to be approximately 0.4 from the experimental data at 298K. Figure 13b shows the resulting temperature dependent $\tau_{CRSS\text{-}slip}$. Interestingly, the estimated critical resolved shear stress at 77K is then equal to 156.6MPa and falls in between the range provided according the experiment results obtained from the single crystal experiments (Fig. 11a).

4 Discussion

In this work, an equiatomic CoCrNi medium entropy alloy was casted and successively homogenized and solution-treated to obtain a coarse-grained microstructure (Fig. 4a). As observed from the EDX analysis (Fig.1), a homogeneous chemical composition was achieved. X-ray analysis shows clear diffraction peaks (Fig. 2) characterizing a cubic fcc single phase with lattice parameter a = 3.55Å. Through a series of experiments which included incremental loading at room temperatures, as well as at cryogenic temperatures, the active deformation mechanisms at the onset of plasticity was thoroughly investigated. High-resolution DIC strain measurements and EBSD data were utilized to provide a clear and quantitative assessment of the buildup of plastic strains post yielding across a relatively large area (≈ 2×2 mm), at both 298K and 77K temperatures.

At the macroscale, the measured room temperature (i.e., 298K) yield strength was slightly lower compared to previously reported magnitudes in the literature. The deviation is induced by

the relatively large grain size in the considered coarse-grained microstructure. Yoshida and coworkers provided the Hall-Petch relationship by studying re-crystallized microstructures of CoCrNi subjected to severe plastic deformation (high-pressure torsion). The predicted yield stress based on Yoshida's work for very large grain size approaches the friction stress which was estimated to be 218MPa [30]. In the present study, the yield strength was (194.9± 19.7) MPa which is within 10% of the referenced yield stress. In addition, the results of Wu and coauthors demonstrate higher yield stress for the same composition which was achieved with a refined microstructure and with the presence of annealing twins which imparts additional strengthening [28]. For the coarse-grained microstructure considered in the present study, once the deformation temperature was dropped to 77K, the expected amplification in yield strength was observed and the ratio between the yield stresses at 77K and 298K reaches a value of 2. Wu et al. reported a ratio of approximately 1.7 for CoCrNi with an average grain size of 41μm [28]. Laplanche and coworkers investigated a microstructure having a 16μm average grain diameter which revealed a ratio of 1.56 between the two yield stress values, 360MPa at 298K and 560MPa at 77K [29]. Based on the available experimental observations in the literature and in the current work, the temperature effect on the yield strength is dependent on the grain size, in particular for microstructures with refined and relatively small grain diameters. However, as the grain size increases, the ratio saturates since the resulting temperature dependence of the yield strength is purely dominated by the friction stress. In the case of the present coarse-grained CoCrNi microstructure, this is expected to be the case which would therefore support the conclusion that the temperature dependence in the $\tau_{CRSS\text{-}slip}$ (Fig. 13b) follows the same trend as the yield strength magnitudes reported in Fig. 13a. It should be pointed out that the ratio provided in this study is relatively high for equiatomic fcc alloys and lower than what can be obtained with bcc metals [28].

To further investigate the temperature-dependence of the yield strength and the active deformation mechanisms at low deformation levels (< 10% strain), two incremental experiments were conducted (see Figs. 4 and 6). The local strain heterogeneities were measured post-deformation using high-resolution DIC with an optimized speckle pattern. The process ensured a stable speckle pattern which was unaffected by submerging the specimen in liquid nitrogen for the 77K deformation cycles. The strain maps were then linked to the underlying microstructure to establish a precise correlation between strain data and grain orientation. Following this process, the same microstructure was deformed at two different temperatures, 298K and 77K, to relatively low levels of deformation (average strain < 4% each). The experiment was successively repeated on a second microstructure with a reverse temperature sequence. In both cases it is clearly shown that slip dominated the onset of plasticity and the initial accumulation of permanent plastic strains. In fact, the grain orientations were used to calculate the Schmid factors of the potential slip systems and trace analysis was used to identify the active slip system. Systematically, the shear bands observed to nucleate in the first loading step were also observed to be active in the second load step, independent of the deformation temperature, or sequence. A different deformation mechanism activated due to changing the deformation temperature (i.e., the nucleation of twinning at 77K) would have resulted in a different local strain distribution. This was not clearly observed from the strain maps which show, instead, very similar increment of local strains for both load steps.

In addition to the experiments on the polycrystalline samples, we also performed experiments on two single crystal specimens with orientations conducive to plastic deformation by slip (Figs. 9-11). Through the use of high resolution, full-field, and local strain measurements, accurate assessment of the CRSS was conducted in-situ at 298K ($\tau_{CRSS\text{-}slip}$=78.1MPa). At 77K, as

in-situ DIC measurements are not possible with the specimen being submerged in LN, the CRSS was determined though incremental loading steps and ex-situ DIC. Therefore, the CRSS is reported as a range between two stress limits, before and after the activation of slip ($140MPa \leq \tau_{CRSS-slip} \leq 160MPa$). The ratio between the two $\tau_{CRSS\text{-}slip}$ values at 77K and 298K gives a value of ≈ 2, which is similar to the results obtained from the macroscopic yield stress measurements. This confirms that the onset of yielding (with no deformation history) is dominated by slip and that the temperature dependence is fully dominated by the friction stress. Compared to other values from literature, Uzer and coworkers found a slightly lower resolved shear stress for slip at 298K equal to 69MPa [38], however the difference is limited (less than 13%) and the values are comparable. A remarkable result presented herein is the confirmation of the $\tau_{CRSS\text{-}slip}$ at 298K from the polycrystalline specimen. In particular, sub-grain DIC measurements were implemented to study the local evolution of the deformation in the present coarse microstructure. Fig. 8 shows the results of an incremental test where the polycrystalline specimen was loaded and high-resolution DIC was employed to study the onset of plasticity in the local microstructures. The grains shown in the figure display shear bands, successively indexed as active slip planes, activated under a shear stress lower than 87MPa. This result confirms the measurements performed on the single crystal specimens.

The enhanced ductility of CoCrNi has been typically related with the low stacking fault energy that drives the alloy propensity to deform by twinning [45]. Multiple studies have been dedicated to identify the CRSS for slip and twinning in the Cantor, CoCrNi, and derivatives of these systems in order to better understand the local deformation mechanisms and their effects on hardening rates and ductility levels. A summary of the available experimental data for the CoCrNi, FeCoCrNi and FeCoCrNiMn alloys, with focus on the CRSS for slip and twinning, is shown in

Table 1 and Fig.14. Compared to slip, the twinning temperature-dependence was observed to be almost negligible for CoCrNi, [29] while for other similar compositions, i.e., the FeCoCrNi, the twinning stress was observed to change [46]. Laplanche reported a critical resolved shear stress for twinning of 260±30MPa 30MPa at a nominal true strain between 4% and 6.7%. This value was successively confirmed by Huang and coworkers through an extended twinning nucleation Peierls-Nabarro model that provides for the present equiatomic CoCrNi alloy a value of 291MPa [47]. It is however noteworthy to mention that Uzer and coworkers found a much lower values of $\tau_{CRSS-twin}$=78±5 MPa at nominal strain of 4% for the [110] orientation, and below 10% for the [111] and [123] orientations at room temperature [38]. A large discrepancy in the reported stresses can be observed which might suggest that twinning is favored in single crystals compared to polycrystals. Aside from this discrepancy, the general trends for alloys discussed in Table 1 and summarized in Fig. 14 point to the following conclusions: i) unlike slip, the twinning stress exhibits weak temperature dependence between 77K and 298K; ii) the twinning stress is significantly higher than the slip stress with the difference being strongly temperature dependent due to strong influence from temperature on the slip resistance; iii) the relatively lower slip stress compared to twinning, at the considered temperatures, tends to favor initial deformation by slip, this result was further confirmed in this study (Figs. 9 and 10) based on local strain measurements across a relatively large area. However, with continued deformation and the associated hardening, twinning nucleates once the stress reaches the CRSS for twin nucleation. This is obviously easier to occur at 77K due the significantly higher slip stress which approaches the corresponding twinning stresses as shown in Table 1. Nevertheless, and as discussed previously, the initial yielding and the prediction of the onset of plasticity is dictated by slip with limited contribution from any other deformation mechanisms.

Table 1. Summary of the available experimental measurements for the CRSS for slip and twinning with emphasis on results obtained from single crystalline MEAs and HEAs.

Reference	Material	Grain size (μm)	Temperature (K)	Deformation Mechanism	τ_{CRSS} (MPa)
B. Uzer et al. 2018 [38]	CoCrNi	Single Crystal	293	Slip	69 ± 3
				Twin	78 ± 5
G. Laplanche et al. 2017 [29]	CoCrNi	16	77	Twin	260 ± 30
			293		
Z. Wu et al. 2015 [48]	FeCoCrNi	Single Crystal	77	Slip	96 ± 5
			293		41.4 ± 2
Y. Wang et al. 2018 [46]	FeCoCrNi	35	77	Twin	207.5 ± 9.8
			293		238.7 ± 9.8
L. Patriarca et al. 2016 [39]	FeCoCrNiMn	Single Crystal	77	Slip	175
			293		70
G. Laplanche et al. 2016 [19]	FeCoCrNiMn	17	77	Twin	235 ± 10
			293		
I. V. Kireeva et al. 2017 [23]	FeCoCrNiMn	Single Crystal	293	Slip	80.3 ± 4
				Twin	125 ± 15
W. Abuzaid et al. 2017 [24]	FeCoCrNiMn	Single Crystal	77	Slip	155
				Twin	153
			293	Slip	56
Y. Wu et al. 2018 [27]	FeCoCrNiMn	Single Crystal	77	Twin	164 ± 4

From the previous discussion, it is evident that the macroscopic yield strength and the CRRS for slip were observed to obey the same temperature dependence as both display an increase by a factor of 2 once the temperature is decreased from 298K to 77K. According to this important

result, we presented an analysis of the exponential relation between temperature and yield stress (Fig. 13a) which was presented and validated over a range of high and medium entropy alloys by Wu and coworkers [28]. The fitting of equation 3 indicates that the parameter α, which dictates the temperature dependency, was found to be 0.0007 confirming the value obtained by Wu for the same composition [28]. The a-thermal term σ_b was instead found to be lower in this study, 68MPa versus 167MPa. This difference is considered to be related to the coarse-grained microstructure as previously discussed. Moreover, the validity of the present analysis is further confirmed by the fitted valued of the material constant $\omega_0/b=0.97$ which is very close to the reasonable assumption that for equiatomic alloys the dislocation width at 0K is equal to the magnitude of the Burgers vector $\omega_0=b$ (narrower dislocation width than pure fcc metals). The exponential equation 3, derived for the yield stress, was then used to plot the temperature dependency of $\tau_{CRSS\text{-}slip}$. It was observed that at the temperature of 298K, the ratio between $\tau_{CRSS\text{-}slip}$ and the 0.2% yield stress is 0.4. The same result is obtained at 77K where the yield stress is 391MPa and the $\tau_{CRSS\text{-}slip}$ between 140 and 160MPa giving a ratio of (0.36-0.41). The final plot of temperature versus $\tau_{CRSS\text{-}slip}$ was then obtained by multiplying the yield stress equation by 0.4. Providing an estimate of the CRSS is of great fundamental importance in modeling efforts, in particular to predict the onset of yielding. We emphasize that the use of single crystalline specimens to establish accurate values of the CRSS, and the use of coarse-grained specimens to establish the yield temperature dependence across a wider range of temperatures, was essential in this study.

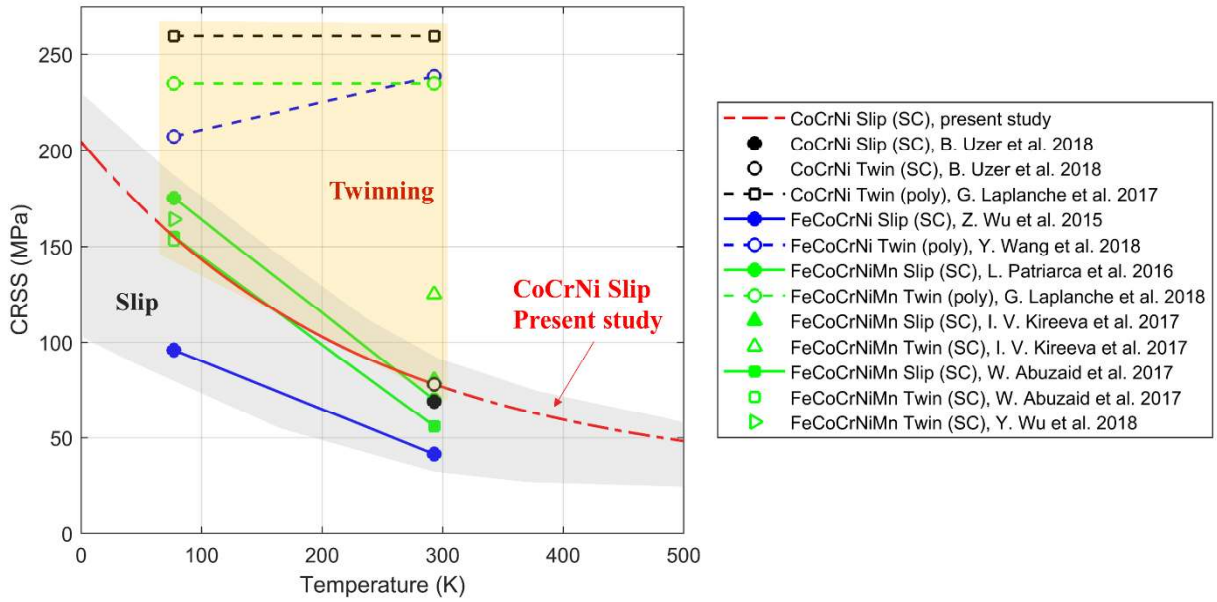

Fig. 14. Trends in the CRSS for twinning and slip for various CoCrNi-based HEA and MEA for single crystal (SC) and polycrystal (poly) specimens.

Conclusions

The work supports the following conclusions:

(1) The critical resolved shear stress for slip for the equiatomic CoCrNi MEA was measured to be 78.1MPa at 298K and between 140MPa and 160MPa at 77K.

(2) The yield stress temperature dependence was correlated with the temperature-dependence of the friction stress. This result, along with discrete CRSS stress measurements at particular temperatures, was used to calculate the critical resolved shear stress for slip in the range of temperatures from 77K to 575K.

(3) In-situ experiments on polycrystalline specimens further confirmed the critical resolved shear stress for slip measured using single crystal specimens. At the deformation levels considered in this work (<10%), the deformation was dominated by plastic slip in the

systems with the largest Schmid factors (at 298K as well as 77K). The corresponding CRSS for slip was calculated to be lower than 90MPa which confirms the results observed from single crystals in this work.

(4) A special experimental procedure was implemented to study the local strain heterogeneities in coarse grained microstructures where two deformation steps were implemented at different temperatures. The results demonstrated that slip dominates the early stages of plastic deformation for both loading steps performed at 77K and 298K indicating also that, despite the heterogeneous local deformations, all the grains display slip deformation which contributes to the large ductility observed in the high entropy alloy.

Acknowledgments

The authors would like to acknowledge the support of the American University of Sharjah (EFRG18-MSE-CEN-22) and Politecnico di Milano as part of the experimental activities were carried out in the METAMAT-Laboratory led by Prof. S. Beretta.

References:

[1] Z. Lyu, X. Fan, C. Lee, S.-Y. Wang, R. Feng, P.K. Liaw, Fundamental understanding of mechanical behavior of high-entropy alloys at low temperatures: A review, J. Mater. Res. (2018) 1–13. doi:10.1557/jmr.2018.273.

[2] E.J. Pickering, N.G. Jones, High-entropy alloys: a critical assessment of their founding principles and future prospects, Int. Mater. Rev. 61 (2016) 183–202.

[3] J.-W. Yeh, S.-K. Chen, S.-J. Lin, J.-Y. Gan, T.-S. Chin, T.-T. Shun, C.-H. Tsau, S.-Y. Chang, Nanostructured High-Entropy Alloys with Multiple Principal Elements: Novel Alloy Design Concepts and Outcomes, Adv. Eng. Mater. 6 (2004) 299–303. doi:10.1002/adem.200300567.

[4] Y. Zhang, T.T. Zuo, Z. Tang, M.C. Gao, K.A. Dahmen, P.K. Liaw, Z.P. Lu, Microstructures and properties of high-entropy alloys, Prog. Mater. Sci. 61 (2014) 1–93. doi:10.1016/J.PMATSCI.2013.10.001.

[5] M.-H. Tsai, J.-W. Yeh, High-Entropy Alloys: A Critical Review, Mater. Res. Lett. 2 (2014) 107–123. doi:10.1080/21663831.2014.912690.

[6] J.-W. Yeh, Alloy Design Strategies and Future Trends in High-Entropy Alloys, JOM. 65 (2013) 1759–1771. doi:10.1007/s11837-013-0761-6.

[7] Y.F. Ye, Q. Wang, J. Lu, C.T. Liu, Y. Yang, High-entropy alloy: challenges and prospects, Mater. Today. 19 (2016) 349–362. doi:10.1016/J.MATTOD.2015.11.026.

[8] B. Cantor, Cantor, Brian, Multicomponent and High Entropy Alloys, Entropy. 16 (2014) 4749–4768. doi:10.3390/e16094749.

[9] H.Y. Diao, R. Feng, K.A. Dahmen, P.K. Liaw, Fundamental deformation behavior in high-entropy alloys: An overview, Curr. Opin. Solid State Mater. Sci. 21 (2017) 252–266. doi:10.1016/J.COSSMS.2017.08.003.

[10] M.C. Gao, J.-W. Yeh, P.K. Liaw, Y. Zhang, High-entropy alloys: fundamentals and applications, Springer, 2016.

[11] B.S. Murty, J.-W. Yeh, S. Ranganathan, P.P. Bhattacharjee, High-entropy alloys, Elsevier, 2019.

[12] D.B. Miracle, O.N. Senkov, A critical review of high entropy alloys and related concepts, Acta Mater. 122 (2017) 448–511. doi:10.1016/J.ACTAMAT.2016.08.081.

[13] Z. Li, S. Zhao, R.O. Ritchie, M.A. Meyers, Mechanical properties of high-entropy alloys with emphasis on face-centered cubic alloys, Prog. Mater. Sci. 102 (2019) 296–345. doi:10.1016/J.PMATSCI.2018.12.003.

[14] B. Cantor, I.T.H. Chang, P. Knight, A.J.B. Vincent, Microstructural development in equiatomic multicomponent alloys, Mater. Sci. Eng. A. 375–377 (2004) 213–218. doi:10.1016/J.MSEA.2003.10.257.

[15] B. Gludovatz, A. Hohenwarter, D. Catoor, E.H. Chang, E.P. George, R.O. Ritchie, A fracture-resistant high-entropy alloy for cryogenic applications, Science (80-.). 345

(2014) 1153–1158. doi:10.1126/science.1254581.

[16] W. Wu, S. Ni, Y. Liu, B. Liu, M. Song, Amorphization at twin-twin intersected region in FeCoCrNi high-entropy alloy subjected to high-pressure torsion, Mater. Charact. 127 (2017) 111–115. doi:10.1016/J.MATCHAR.2017.02.027.

[17] R. Raghavan, C. Kirchlechner, B.N. Jaya, M. Feuerbacher, G. Dehm, Mechanical size effects in a single crystalline equiatomic FeCrCoMnNi high entropy alloy, Scr. Mater. 129 (2017) 52–55. doi:10.1016/J.SCRIPTAMAT.2016.10.026.

[18] I. Kireeva, Y. Chumlyakov, Z. Pobedennaya, D. Kuksgauzen, I. Karaman, H. Sehitoglu, Mechanisms of plastic deformation in [1¯11]-oriented single crystals of FeNiMnCrCo high entropy alloy, in: AIP Conf. Proc., AIP Publishing LLC, 2016: p. 020090. doi:10.1063/1.4966383.

[19] G. Laplanche, A. Kostka, O.M. Horst, G. Eggeler, E.P. George, Microstructure evolution and critical stress for twinning in the CrMnFeCoNi high-entropy alloy, Acta Mater. 118 (2016) 152–163. doi:10.1016/J.ACTAMAT.2016.07.038.

[20] F. Otto, A. Dlouhý, C. Somsen, H. Bei, G. Eggeler, E.P. George, The influences of temperature and microstructure on the tensile properties of a CoCrFeMnNi high-entropy alloy, Acta Mater. 61 (2013) 5743–5755. doi:10.1016/J.ACTAMAT.2013.06.018.

[21] Z. Zhang, M.M. Mao, J. Wang, B. Gludovatz, Z. Zhang, S.X. Mao, E.P. George, Q. Yu, R.O. Ritchie, Nanoscale origins of the damage tolerance of the high-entropy alloy CrMnFeCoNi, Nat. Commun. 6 (2015) 10143.

[22] B. Gludovatz, E.P. George, R.O. Ritchie, Processing, microstructure and mechanical properties of the CrMnFeCoNi high-entropy alloy, JOM. 67 (2015) 2262–2270.

[23] I.V. Kireeva, Y.I. Chumlyakov, Z.V. Pobedennaya, I.V. Kuksgausen, I. Karaman, Orientation dependence of twinning in single crystalline CoCrFeMnNi high-entropy alloy, Mater. Sci. Eng. A. 705 (2017) 176–181. doi:10.1016/J.MSEA.2017.08.065.

[24] W. Abuzaid, H. Sehitoglu, Critical resolved shear stress for slip and twin nucleation in single crystalline FeNiCoCrMn high entropy alloy, Mater. Charact. 129 (2017) 288–299. doi:10.1016/j.matchar.2017.05.014.

[25] M. Bönisch, Y. Wu, H. Sehitoglu, Hardening by slip-twin and twin-twin interactions in FeMnNiCoCr, Acta Mater. 153 (2018) 391–403. doi:10.1016/J.ACTAMAT.2018.04.054.

[26] S. Alkan, A. Ojha, H. Sehitoglu, Determination of latent hardening response for FeNiCoCrMn for twin-twin interactions, Acta Mater. 147 (2018) 149–164. doi:10.1016/J.ACTAMAT.2017.12.058.

[27] Y. Wu, M. Bönisch, S. Alkan, W. Abuzaid, H. Sehitoglu, Experimental determination of latent hardening coefficients in FeMnNiCoCr, Int. J. Plast. 105 (2018) 239–260. doi:10.1016/J.IJPLAS.2018.02.016.

[28] Z. Wu, H. Bei, G.M. Pharr, E.P. George, Temperature dependence of the mechanical properties of equiatomic solid solution alloys with face-centered cubic crystal structures, Acta Mater. 81 (2014) 428–441. doi:10.1016/J.ACTAMAT.2014.08.026.

[29] G. Laplanche, A. Kostka, C. Reinhart, J. Hunfeld, G. Eggeler, E.P. George, Reasons for the superior mechanical properties of medium-entropy CrCoNi compared to high-entropy CrMnFeCoNi, Acta Mater. 128 (2017) 292–303.

[30] S. Yoshida, T. Bhattacharjee, Y. Bai, N. Tsuji, Friction stress and Hall-Petch relationship in CoCrNi equi-atomic medium entropy alloy processed by severe plastic deformation and subsequent annealing, Scr. Mater. 134 (2017) 33–36.

[31] I. Moravcik, J. Cizek, Z. Kovacova, J. Nejezchlebova, M. Kitzmantel, E. Neubauer, I. Kubena, V. Hornik, I. Dlouhy, Mechanical and microstructural characterization of powder metallurgy CoCrNi medium entropy alloy, Mater. Sci. Eng. A. 701 (2017) 370–380.

[32] C.E. Slone, S. Chakraborty, J. Miao, E.P. George, M.J. Mills, S.R. Niezgoda, Influence of deformation induced nanoscale twinning and FCC-HCP transformation on hardening and texture development in medium-entropy CrCoNi alloy, Acta Mater. 158 (2018) 38–52. doi:10.1016/J.ACTAMAT.2018.07.028.

[33] Y.L. Zhao, T. Yang, Y. Tong, J. Wang, J.H. Luan, Z.B. Jiao, D. Chen, Y. Yang, A. Hu, C.T. Liu, J.-J. Kai, Heterogeneous precipitation behavior and stacking-fault-mediated deformation in a CoCrNi-based medium-entropy alloy, Acta Mater. 138 (2017) 72–82. doi:10.1016/J.ACTAMAT.2017.07.029.

[34] B. Gludovatz, A. Hohenwarter, K.V.S. Thurston, H. Bei, Z. Wu, E.P. George, R.O. Ritchie, Exceptional damage-tolerance of a medium-entropy alloy CrCoNi at cryogenic temperatures, Nat. Commun. 7 (2016) 10602.

[35] J. Miao, C.E. Slone, T.M. Smith, C. Niu, H. Bei, M. Ghazisaeidi, G.M. Pharr, M.J. Mills, The evolution of the deformation substructure in a Ni-Co-Cr equiatomic solid solution alloy, Acta Mater. 132 (2017) 35–48. doi:10.1016/J.ACTAMAT.2017.04.033.

[36] Z. Zhang, H. Sheng, Z. Wang, B. Gludovatz, Z. Zhang, E.P. George, Q. Yu, S.X. Mao, R.O. Ritchie, Dislocation mechanisms and 3D twin architectures generate exceptional strength-ductility-toughness combination in CrCoNi medium-entropy alloy, Nat. Commun. 8 (2017).

[37] S. Huang, H. Huang, W. Li, D. Kim, S. Lu, X. Li, E. Holmström, S.K. Kwon, L. Vitos, Twinning in metastable high-entropy alloys, Nat. Commun. 9 (2018) 2381. doi:10.1038/s41467-018-04780-x.

[38] B. Uzer, S. Picak, J. Liu, T. Jozaghi, D. Canadinc, I. Karaman, Y.I. Chumlyakov, I. Kireeva, On the mechanical response and microstructure evolution of NiCoCr single crystalline medium entropy alloys, Mater. Res. Lett. 6 (2018) 442–449. doi:10.1080/21663831.2018.1478331.

[39] L. Patriarca, A. Ojha, H. Sehitoglu, Y.I. Chumlyakov, Slip nucleation in single crystal FeNiCoCrMn high entropy alloy, Scr. Mater. 112 (2016) 54–57. doi:10.1016/J.SCRIPTAMAT.2015.09.009.

[40] J.D. Carroll, W.Z. Abuzaid, J. Lambros, H. Sehitoglu, On the interactions between strain accumulation, microstructure, and fatigue crack behavior, Int. J. Fract. 180 (2013) 223–241. doi:10.1007/s10704-013-9813-8.

[41] W. Abuzaid, A. Oral, H. Sehitoglu, J. Lambros, H.J. Maier, Fatigue crack initiation in Hastelloy X - the role of boundaries, Fatigue Fract. Eng. Mater. Struct. 36 (2013) 809–826. doi:10.1111/ffe.12048.

[42] Y. Guan, B. Chen, J. Zou, T. Ben Britton, J. Jiang, F.P.E. Dunne, Crystal plasticity modelling and HR-DIC measurement of slip activation and strain localization in single and oligo-crystal Ni alloys under fatigue, Int. J. Plast. 88 (2017) 70–88. doi:10.1016/J.IJPLAS.2016.10.001.

[43] Effects of temperature on the plastic properties of aluminium crystals, Proc. R. Soc. London. Ser. A. Math. Phys. Sci. 233 (1955) 17–34. doi:10.1098/rspa.1955.0243.

[44] J. Carroll, W. Abuzaid, J. Lambros, H. Sehitoglu, An experimental methodology to relate local strain to microstructural texture, Rev. Sci. Instrum. 81 (2010). doi:10.1063/1.3474902.

[45] Y. Ikeda, B. Grabowski, F. Körmann, Ab initio phase stabilities and mechanical properties of multicomponent alloys: A comprehensive review for high entropy alloys and compositionally complex alloys, Mater. Charact. 147 (2019) 464–511. doi:10.1016/J.MATCHAR.2018.06.019.

[46] Y. Wang, B. Liu, K. Yan, M. Wang, S. Kabra, Y.L. Chiu, D. Dye, P.D. Lee, Y. Liu, B. Cai, Probing deformation mechanisms of a FeCoCrNi high-entropy alloy at 293 and 77 K using in situ neutron diffraction, Acta Mater. 154 (2018) 79–89. doi:10.1016/j.actamat.2018.05.013.

[47] H. Huang, X. Li, Z. Dong, W. Li, S. Huang, D. Meng, X. Lai, T. Liu, S. Zhu, L. Vitos, Critical stress for twinning nucleation in CrCoNi-based medium and high entropy alloys, Acta Mater. 149 (2018) 388–396. doi:10.1016/J.ACTAMAT.2018.02.037.

[48] Z. Wu, Y.F. Gao, H. Bei, Single crystal plastic behavior of a single-phase, face-center-cubic-structured, equiatomic FeNiCrCo alloy, Scr. Mater. 109 (2015) 108–112. doi:10.1016/J.SCRIPTAMAT.2015.07.031.